IOP Publishing
Plasma Sources Science and Technology
Plasma Sources Sci. Technol. **23** (2014) 044004 (9pp)
doi:10.1088/0963-0252/23/4/044004

Effect of magnetic and physical nozzles on plasma thruster performance

Kazunori Takahashi[1], **Christine Charles**[2], **Rod Boswell**[2] **and Akira Ando**[1]

[1] Department of Electrical Engineering, Tohoku University, Sendai 980-8579, Japan
[2] Space Plasma, Power and Propulsion Laboratory, Research School of Physics and Engineering,
The Australian National University, Canberra ACT 0200, Australia

E-mail: kazunori@ecei.tohoku.ac.jp

Received 29 August 2013, revised 23 November 2013
Accepted for publication 10 December 2013
Published 22 July 2014

Abstract

Plasma cross-field diffusion in a magnetic nozzle is inhibited by increasing the magnetic field strength in a helicon plasma thruster attached to a pendulum thrust balance, while maintaining constant plasma density and electron temperature in the source tube, i.e. a constant plasma injection into the magnetic nozzle, where the field strength near the radio frequency (rf) antenna is less than 210 G and the operating argon pressure in the vacuum chamber is 0.8 mTorr. Inhibition of the cross-field diffusion yields a higher electron pressure in the magnetic nozzle and a resultant larger thrust. The thrust component arising from the magnetic nozzle approaches the theoretical limit derived from an ideal magnetic nozzle approximation where no plasma is lost from the nozzle and there is an azimuthal plasma current originating from the electron diamagnetic drift. It is also shown that the momentum of the plasma lost from the magnetic nozzle is captured by a physical nozzle attached at the source exit resulting in a larger thrust. Two physical nozzles of different sizes (nozzle 1: 10.5 cm in length with a maximum diameter of 20 cm, nozzle 2: 26 cm in length with a maximum diameter of 36 cm) are tested. The maximum thrust of 20 ± 1 mN is obtained for 25 sccm argon propellant and 2 kW rf power with a reflection power less than 5 W, which gives a specific impulse of 2750 ± 165 s and a thrust efficiency of 13.5 ± 1.5%.

Keywords: helicon plasma thruster, magnetic nozzle, physical nozzle, thrust measurement, plasma momentum, cross-field diffusion

(Some figures may appear in colour only in the online journal)

1. Introduction

Momentum, i.e. thrust imparted from electric propulsion devices, is an important physical quantity used in assessing the performance of thrusters. The performance of conventional electric propulsion devices such as MPD arc jets [1–3], Hall effect thrusters [4–6] and ion gridded thrusters [4, 7, 8] has been measured and theoretical models have been developed, which incorporate the beam extraction parameters or the interaction between magnetic field and discharge current. In such devices, electrodes for plasma production and/or acceleration are exposed to the plasma and can be damaged by ion sputtering and thermal load; hence the development of electrodeless plasma thrusters such as the Variable Specific Impulse Magnetoplasma Rocket (VASIMR) [9], the helicon plasma thruster including the helicon double layer thruster (HDLT) [10, 11] and the radio frequency (rf) plasma thruster [12] has been proposed. The direct measurements of the thrust imparted from the helicon plasma thruster, operated below a few kW, started only a few years ago using thrust balances [13–16]. The magnetic field applied to the helicon plasma thruster principally plays two roles in the device operation. One is enabling an efficient rf power coupling via a helicon wave, which can propagate in plasmas immersed in a static magnetic field [17]; another is the formation of a magnetic nozzle downstream of the thruster exit [18]. The performance of the magnetic nozzle plasma thruster has also been analytically investigated and gives thrust components arising from the plasma pressure (mainly electron pressure) force onto the axial source boundary and from the Lorentz force due to the azimuthal plasma current and the applied radial magnetic field [18–21]. The former and latter components have been experimentally verified using a simple inductively coupled plasma thruster [22] and by independently measuring the thrust component arising from the magnetic nozzle [20]. The theoretical studies have now extended into plasma cross-field diffusion [23] and plasma detachment from the magnetic nozzle [24]. Plasma flow and instabilities in the magnetic nozzle have also been investigated by particle-in-cell simulations [25]. A recent experiment has briefly shown the influence of the cross-field diffusion and the resultant plasma loss from the magnetic nozzle on the thrust [26], where it was observed that the thrust increases up to 10–11 mN for 1 kW rf power when increasing the magnetic field strength. Hence the key issue in improving the helicon thruster performance is how to inhibit the plasma cross-field diffusion in the magnetic nozzle. Some high-beta helicon experiments have shown modification of the applied magnetic field lines by the plasma current [27], which might be connected to the plasma detachment phenomena, where the beta is defined as a ratio between the plasma pressure and the magnetic pressure.

Here experiments are conducted on controlling the plasma cross-field diffusion by the magnetic field strength while maintaining a constant plasma production in a low-beta helicon plasma thruster thus allowing the thrust components arising from the axial and radial source boundaries and the magnetic nozzle to be directly measured. The thruster is designed to have a magnetic field strength less than 210 G near the rf antenna so as to maintain an ion Larmor radius larger than or comparable to the source tube radius; an unchanged plasma density in the source tube is observed for these conditions. Some of these results have been reported briefly in a previous paper [26] and the detailed results are described here. Furthermore, an effect of physical nozzle attached at the thruster exit is experimentally investigated and the thruster performance is successfully improved.

2. Experimental setup

Experiments are performed using a helicon plasma thruster attached to a pendulum thruster balance immersed in a 60 cm-diameter and 140 cm-long vacuum chamber shown in figure 1(*a*), and the detailed structure of the thruster is shown in figure 1(*b*). The chamber is evacuated to a base pressure of 10^{-6} Torr by a turbomolecular/rotary pumping system (effective pumping speed for argon is $400\,\mathrm{l\,s^{-1}}$). The thruster cavity shown in figure 1(*b*) is a 6.4 cm-inner-diameter and 20 cm-long pyrex glass tube. $z = 0$ is defined as the open exit of the source tube and the ‘upstream’ end of the source tube ($z = -20$ cm) is terminated by an insulator back plate with a 6 mm-diameter center hole. Argon propellant is introduced via the center hole of the back plate using a 1 mm-inner diameter and 2 mm-outer diameter ceramic tube. In the present experiments the argon flow rate is maintained at 25 sccm ($0.75\,\mathrm{mg\,s^{-1}}$) using a mass flow controller with an uncertainty of ±1% in the flow rate; the chamber pressure measured by a baratron gauge connected to a side port of the chamber was 0.8 mTorr and the electron–neutral collision mean free path is roughly estimated as ∼65 cm assuming a collisional cross-section of $\sim 6 \times 10^{-20}\,\mathrm{m^{-2}}$ [28]. A 10 cm-inner diameter, 16.4 cm-outer diameter and 5 cm wide solenoid with 560 turns is centered at $z = -3.4$ cm to create a magnetic nozzle using a solenoid current of up to $I_B = 15$ A. The calculated magnetic field strength $|B|$ in the x–z plane and on axis for $I_B = 15$ A are shown by color contours in figure 1(*b*) and by a solid line in figure 2, respectively. The white solid lines in figure 1(*b*) are calculated magnetic field lines. The magnetic field strength peaks at about 760 G at $z = -3.4$ cm and rapidly decreases towards the upstream and downstream sides of the plasma cavity. A 8 cm inner-diameter double-turn rf loop antenna, made of a 6 mm-diameter copper tube and shielded by a thick ceramic ring and grounded metallic parts to prevent any parasitic discharges outside of the source tube as described in [29], is located at $z = -11.5$ cm and powered by a 13.56 MHz rf generator via an impedance matching circuit consisting of three capacitors as shown in figure 1(*c*). The argon ion Larmor radius calculated for the maximum solenoid current $I_B = 15$ A assuming an ion temperature of 0.2 eV is shown by a dotted line in figure 2. The ion Larmor radius at the rf antenna position ($z_{\mathrm{ant}} = -11.5$ cm) is about 2.2 cm for the magnetic field strength of 210 G. Here the ion Larmor radius is comparable to or larger than the source tube radius (for smaller solenoid currents) and no significant change in the plasma loss rate onto the radial source wall is expected and a constant plasma production is maintained as described in section 4.

To investigate plasma cross-field diffusion in particular radial loss across the magnetic nozzle, the experiment is also designed to accommodate the addition of a physical nozzle attached to the thruster exit plane as shown in figures 1(*a*) and (*b*). Two different sized physical nozzles made of 0.2 mm thick stainless steel plate are used: a small physical nozzle (labeled ‘nozzle 1’) with 9 cm diameter at $z = 0$ cm and 20 cm diameter at $z = 10.5$ cm and a large nozzle (labeled ‘nozzle 2’) with 9 cm diameter at $z = 0$ cm and 36 cm diameter at $z = 26$ cm.

The thrust is equal in magnitude and opposite in direction to the axial force exerted on the source structure and directly measured using a pendulum thrust balance, as shown in figure 1(*a*), which has been briefly described in [26]. The helicon plasma thruster is attached to the balance, while the rf antenna and gas feedthrough are mounted on mechanical structures connected to the inner wall of the vacuum chamber and are mechanically isolated from the balance. As the plasma is not in contact with the rf antenna and the contact cross-section of the gas feedthrough is much smaller than the source back plate area, the forces imparted from the plasma to these two components are negligible. The displacement of the source structure during plasma production is measured using a laser displacement sensor. Prior to performing displacement measurements, the variable capacitors in the rf matching circuit are pre-tuned to minimize rf power reflection from the impedance matching circuit including the antenna and plasma loads (less than 5 W reflection for 2 kW rf power input). The typical raw displacement signal from the laser sensor is plotted as a thin line in figure 3. The laser system, magnetic field and plasma are successively turned on at $t \sim 0$ s, 10 s and 18 s,

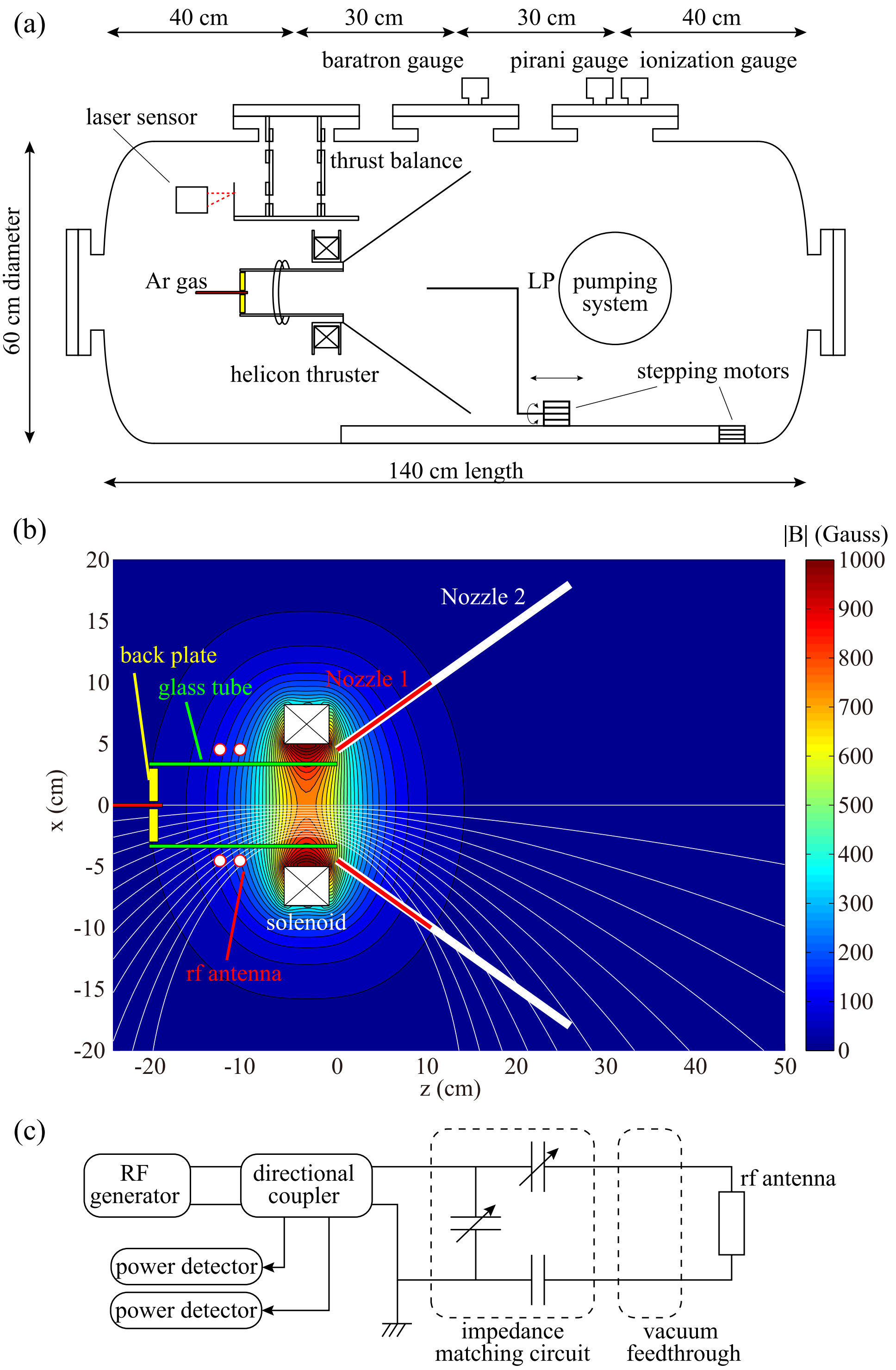

Figure 1. (*a*) Schematic diagram of the experimental setup. (*b*) Schematic diagram of the helicon plasma thruster. The color contours show the calculated magnetic field strength $|B|$ in gauss for $I_B = 15$ A (maximum value used in the present experiment), and the white lines show the magnetic field lines. (*c*) Schematic diagram of the rf circuit.

respectively. The displacement data are acquired for about 5 s before reversing the steps (plasma, magnetic field and laser system successively off at $t \sim 25$ s, 32 s and 50 s, respectively). The shift in the equilibrium positions measured with the plasma on and off corresponds to the displacement resulting from the plasma force. As the rf generator and the subsequent plasma production reach steady state within 0.5 s, the data acquisition for about 5 s is enough to estimate the equilibrium positions during the steady-state thruster operation. As seen in the raw displacement signal (thin line) in figure 3, the pendulum thrust balance has an oscillating component of about 1 Hz, which depends on the weight of the thruster components attached to the balance. To minimize the estimation error of the equilibrium positions, the oscillating component is

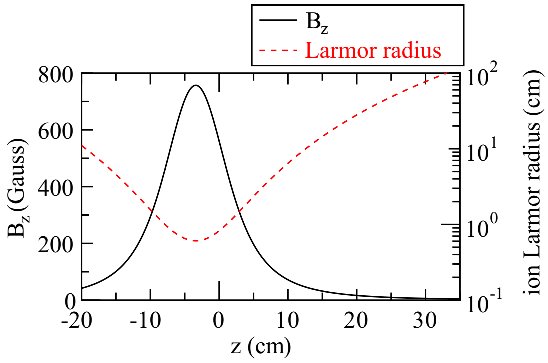

Figure 2. Calculated axial profile of the magnetic field strength for $x = 0$ cm on the axis (solid line) and ion Larmor radius (dotted line) assuming an ion temperature of 0.2 eV for $I_B = 15$ A.

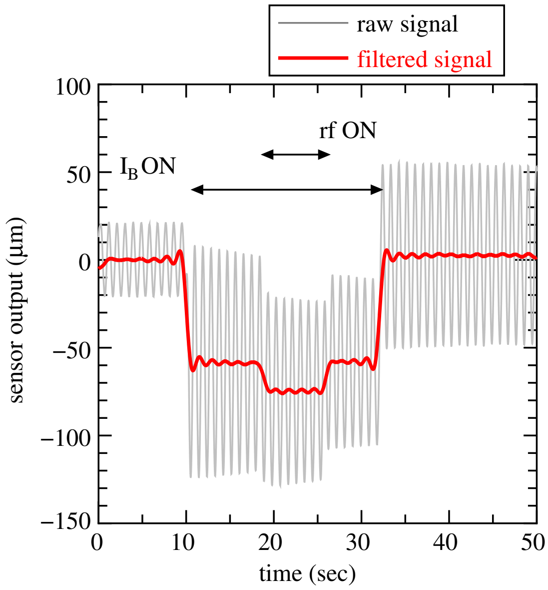

Figure 3. Typical raw (thin solid line) and filtered (bold solid line) displacement curves from the laser sensor where the solenoid current and the rf power are turned on for the $t \sim 10$–33 s and $t \sim 18$–26 s periods, respectively.

filtered by using Fourier analysis and plotted by a bold line in figure 3; then the displacement caused by the plasma force can be obtained with an error less than ±5%. The absolute value of thrust is obtained using a calibration coefficient relating the displacement to the force carried out before pump down and verified after venting the chamber. During the thrust measurements, a Langmuir probe (LP) described later is located at $(x, z) = (20\,\text{cm}, 40\,\text{cm})$. In addition, as no noticeable change in the measured displacement was observed when moving the LP position, the thruster operation is not significantly affected by the presence of the LP.

As described later in section 3 the total thrust is the sum of three components and written as $T_{\text{total}} = T_s + T_w + T_B$ where T_s is the force onto the axial source boundary (back plate in figure 1(*b*)), T_w is the axial force in the radial wall boundary (glass tube in figure 1(*b*)) and T_B is the Lorentz force onto the magnetic nozzle (solenoid on figure 1(*b*)). The present experimental setup has been designed so that these three components can be independently measured by attaching either the source back plate, glass source tube or solenoid to the thrust balance. The total thrust T_{total} is also measured by connecting all three components to the balance.

The 3 mm-diameter planar LP with a dog-leg shaft is mounted on a computer-controlled stepping motor system, as shown in figure 1(*a*); one of the motor stages connected with the probe shaft is moved along the z-axis and the rotation of the shaft yields the radial measurement. The probe voltage is swept from −90 to ∼70 V and the electron temperature (T_e) can be obtained by fitting its semi-log plot to a linear line. The plasma density (n_p) is obtained from the ion saturation current, taking into account the sheath expansion around the probe tip [22]. The effects of the applied magnetic field are currently neglected for the data analysis. The uncertainty of the T_e estimation is less than ±15% and the error in the ion current measurement is less than ±5%. Hence the estimation uncertainty for the plasma density is about ±15%.

3. Thrust modeling

In this section, a simple analytical model of the thrust imparted from the magnetically expanding plasma, previously detailed in [30, 31], is used. Assuming an axisymmetric plasma, negligible electron inertia, negligible radial ion inertia and cold ions, the total thrust corresponding to the axial plasma momentum emitted from the thruster is given by $T_{\text{total}} = T_s + T_w + T_B$, where

$$T_s = 2\pi \int_0^{r_s} r p_e(r, z_0)\, \mathrm{d}r, \tag{1}$$

$$T_w = -2\pi \int_{z_{\text{end}}}^{0} r_s m n_w u_r(r_s, z) u_z(r_s, z)\, \mathrm{d}z, \tag{2}$$

$$T_B = -2\pi \int_0^{z} \int_0^{r_p(z)} r \frac{B_r(r, z)}{B_z(r, z)} \frac{\partial p_e(r, z)}{\partial r}\, \mathrm{d}r\, \mathrm{d}z. \tag{3}$$

r_s, r_p, z_0, n_w, u are the source tube radius, plasma radius, axial position at maximum electron pressure, ion density at the radial wall boundary and ion velocity, respectively.

T_s in equation (1) corresponds to the maximum electron pressure integrated over the source tube cross-section. The net axial momentum at any position z is given by the sum of the static electron pressure ($n_p k_B T_e$) and the ion dynamic momentum ($m n_p u_z^2$). The latter is equal to zero at z_0 since the ion drift velocity is zero at the axial plasma density maximum. The axial electron pressure force acts onto the axial source boundary (back plate on figure 1) via ion acceleration in the sheath and conversion of electron pressure into ion dynamic momentum. Hence the present experimental setup allows the direct measurement of the force exerted onto the axial boundary (back plate), T_s. This term can also be computed using direct LP measurements of the maximum electron pressure within the cavity. T_w in equation (2) shows the surface integration of the axial momentum ($m u_z$) delivered by the ions lost to the radial source boundary, where the ion flux to the radial wall is given by $n_w u_r$. Here the present experimental setup allows the direct measurement of the force T_w exerted onto the radial source tube wall. Finally, T_B in equation (3) represents the volume integration of the Lorentz force resulting from the radial magnetic field component B_r and the azimuthal electron diamagnetic drift current $B_z^{-1}\partial p_e/\partial r$. Thrust is generated via this downstream plasma acceleration. Again the present configuration allows the direct measurement of the force T_B exerted on the solenoid when only the solenoid is attached to the thrust balance.

Fruchtman *et al* have demonstrated that the thrust component T_B in equation (3) can be simplified using a one-dimensional model assuming the paraxial approximation $B_z(r, z) \simeq B_z(0, z) \equiv B_{z0}(z)$ to read [31]

$$T_B \simeq -\int_0^z \langle p_e(z)\rangle A(z)\frac{1}{B_{z0}}\frac{\partial B_{z0}}{\partial z}\,dz. \tag{4}$$

This approximation leads to an underestimation of T_B by $\sim$20% compared with the two-dimensional model of equation (3). $\langle p_e(z)\rangle$ and $A(z)$ are the radially averaged electron pressure and plasma cross-sectional area, respectively. Considering an 'ideal' magnetic nozzle expansion with no radial plasma loss (no cross-field diffusion) and with a plasma radius increase as $r_p(z) = r_s\sqrt{B_{exit}/B_{z0}}$, the value of $\langle p_e(z)\rangle A(z)$ is conserved along z and equal to the value at the source exit $\langle p_{exit}\rangle A_{exit}$. Given the radial profile of electron pressure at the source exit and the magnetic field strength B_{z0} on the axis (figure 2), the theoretical limit of the T_B component for an ideal nozzle, $T_{B\ \mathrm{ideal}}$, is

$$T_{B\ \mathrm{ideal}} \simeq -\int_0^z \langle p_{exit}\rangle A_{exit}\frac{1}{B_{z0}}\frac{\partial B_{z0}}{\partial z}\,dz. \tag{5}$$

4. Results and discussions

Figure 4 shows the axial profiles of (*a*) the plasma density and (*b*) the electron temperature on the axis with the solenoid current I_B as a parameter for no physical nozzle configuration and rf power of 1 kW. For all values of I_B, the profiles of figure 4(*a*) have a density maximum near the rf antenna position of $z \sim -12$ cm. The density on the axis for no magnetic field ($I_B = 0$ A) is asymmetric while it becomes more symmetric within the source cavity ($z < 0$) when the magnetic field is applied. Above 2 A, no measurable change of the density in the source tube is seen, while for $z > 10$ cm the density clearly increases as I_B is increased as seen in figure 4(*a*). The electron temperature in figure 4(*b*) is fairly uniform on axis within the source cavity ($z < 0$) at about 6 ± 1 eV and gradually decreases along the z-axis to values of $\sim$3 eV at $z \sim 40$ cm; this decrease in the electron temperature being invariant with the magnetic field. Although the physical mechanism of the electron cooling along the magnetic nozzle is still unclear, one possible reason is the adiabatic cooling of the electrons suggested by Arefiev and Breizman [32]. Figures 5(*a*) and (*b*) show the x profiles of the plasma density and electron temperature measured at the axial position of the maximum density (hence the maximum electron pressure) for $I_B = 5$ A (filled squares) and 14 A (open circles) with no noticeable change between the two cases. Hence it can be deduced from figures 4, 5(*a*) and (*b*) that the plasma production is unchanged when the solenoid current is increased since the ion Larmor radius at the rf antenna position remains comparable to or larger than the source tube radius, as described in section 2. Figures 5(*c*) and (*d*) show the x profiles of the plasma density and electron temperature measured for $I_B = 5$ A (filled squares) and 14 A (open circles) at $z = 8$ cm at the position of the magnetic nozzle. The x profiles show the greater density at $|x| > 10$ cm for $I_B = 5$ A compared with that obtained for the 14 A case. The electron temperature profiles remain unchanged, where the higher electron temperature at $|x| \sim 4$ cm is due to the transport of the energetic electron along the magnetic nozzle as observed in the previous experiment and simulation [33, 34]. The x profile of the density, the increase in the density in the magnetic nozzle (figure 4(*a*)), and the unchanged electron temperature profile show that some of the plasma within the magnetic nozzle diffuses across the field lines and is lost radially from the magnetic nozzle. The radial plasma loss gives rise to the larger decay of the density within the magnetic nozzle.

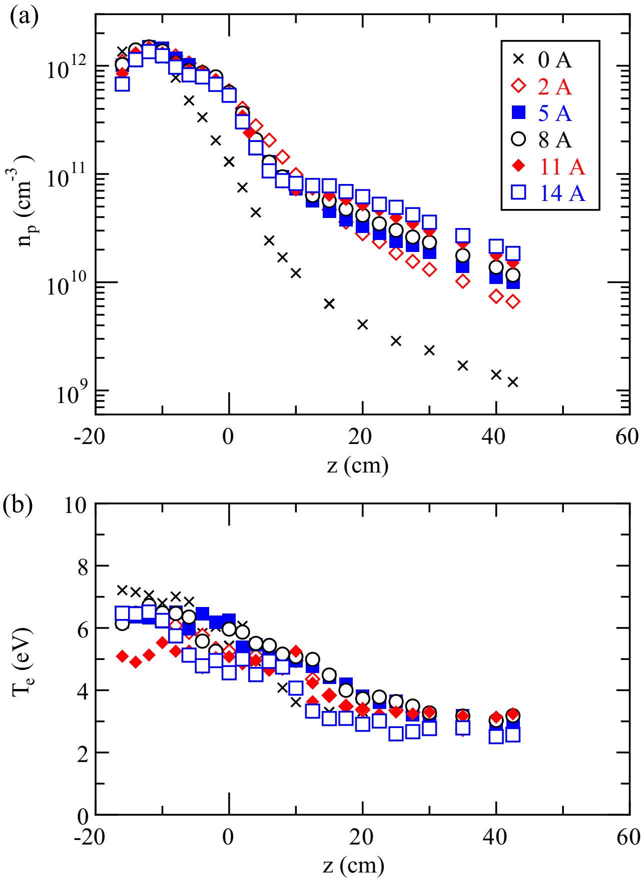

Figure 4. Axial profiles for $x = 0$ cm of (*a*) plasma density and (*b*) electron temperature on the axis for $I_B = 0$ A (crosses), 2 A (open diamonds), 5 A (filled squares), 8 A (open circles), 11 A (filled diamonds) and 14 A (open squares), respectively, with no physical nozzle and rf power of 1 kW. Data for (*a*) are from [26]. Typical errors in both density and temperature estimations are ±15%.

The detailed variation of the plasma density upstream within the source ($z = -12$ cm) and downstream within the magnetic nozzle ($z = 30$ cm) as a function of I_B, respectively, are plotted in figures 6(*a*) and (*c*) as filled circles. When the

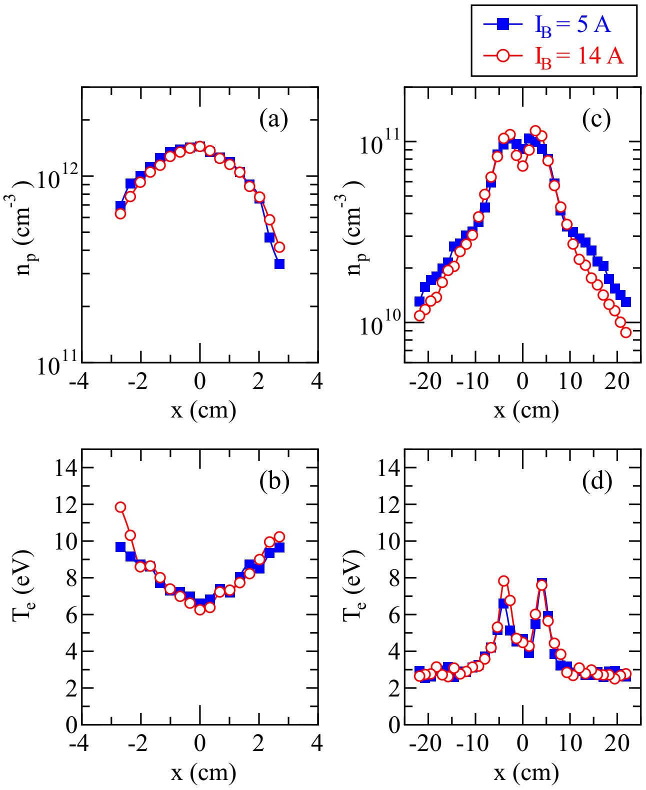

Figure 5. Radial profiles of (*a*), (*c*) plasma density and (*b*), (*d*) electron temperature for $I_B = 5$ A (filled squares) and 14 A (open circles), respectively, with no physical nozzle and rf power of 1 kW. The data in (*a*), (*b*) and (*c*), (*d*) are taken at $z = -12$ cm (within the source tube) and $z = 8$ cm (within the magnetic nozzle), respectively. Data for (*a*) and (*c*) are from [26].

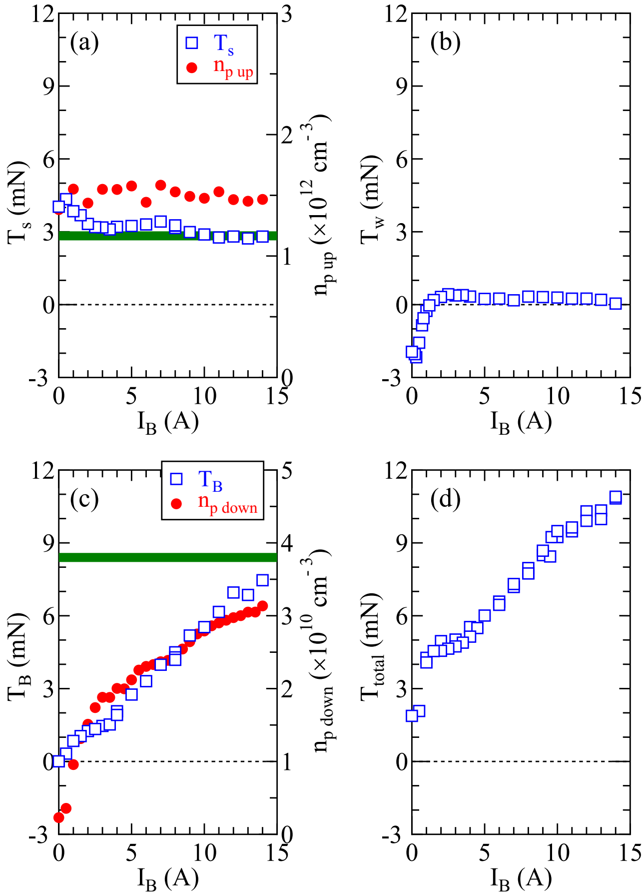

Figure 6. Directly measured values (open squares) of the thrust components (*a*) T_s, (*b*) T_w, (*c*) T_B and (*d*) T_{total} as a function of I_B with no physical nozzle and 1 kW rf power. The filled circles in (*a*) and (*c*) show the plasma density measured at $z = -12$ cm and 30 cm, respectively. T_s calculated from the electron pressure profile in (*a*) and T_B estimated assuming the ideal magnetic nozzle are drawn by bold lines in (*a*) and (*c*), respectively. Data for the figure are from [26]. Typical error in the thrust measurement is within ±5%.

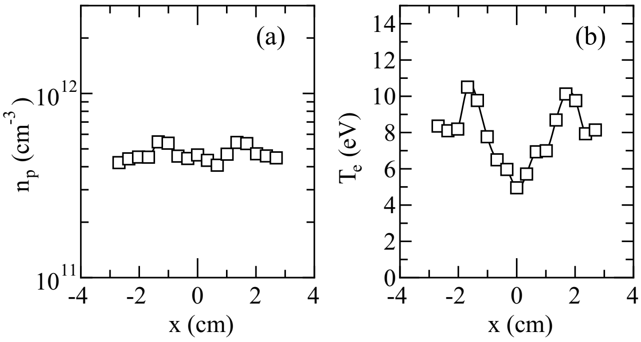

Figure 7. Radial profiles of (*a*) plasma density and (*b*) electron temperature measured at $z = 0$ (source exit) with no physical nozzle, $I_B = 14$ A, and 1 kW rf power.

magnetic field strength is increased from 0 to 14 A solenoid current, the downstream density increases (figure 6(*c*)), while the upstream density is almost constant (figure 6(*a*)). Hence the present experiment demonstrates the decoupling between plasma production and plasma expansion in the magnetic nozzle, and shows that only the cross-field diffusion in the magnetic nozzle can be inhibited by the magnetic field strength while maintaining the constant plasma injection into the magnetic nozzle.

The thrust component T_s given by equation (1) can be calculated from the electron pressure profile at the maximum pressure position ($z_0 = -12$ cm) and the value of T_s calculated for $I_B = 14$ A from the measured profiles (open circles in figures 5(*a*) and (*b*)) is 2.8 ± 0.3 mN and is indicated by a horizontal bold solid line in figure 6(*a*). To calculate the theoretical upper limit of T_B given by equation (5), the radial measurement of the plasma density and electron temperature are performed at the thruster exit ($z = 0$) for $I_B = 14$ A and the results are plotted in figure 7. Substituting the averaged electron pressure at the source exit (which is estimated from the measured profiles in figure 7) and the magnetic field strength on axis B_{z0} into equation (5), the axial profile of $T_{B\ \mathrm{ideal}}$ shown by a solid line in figure 8 is obtained. It is found that the values of $T_{B\ \mathrm{ideal}}$ increases along the z-axis. The dotted line in figure 8 shows the estimated plasma radius r_p according to the procedure in section 3 and reaches the chamber radius of 30 cm at $z = 29.3$ cm. As the theoretical limit of T_B should be that computed for a plasma radius approaching the chamber radius, the value of $T_{B\ \mathrm{ideal}}$ is about 8.4 mN and is indicated by a horizontal bold solid line in figure 6(*c*).

The thrust components T_s, T_w and T_B and the total thrust T_{total} are directly measured for the same condition as in figure 4 as a function of I_B and the results are plotted in figures 6(*a*)–(*d*), respectively, as open squares. The measured T_{total} agrees

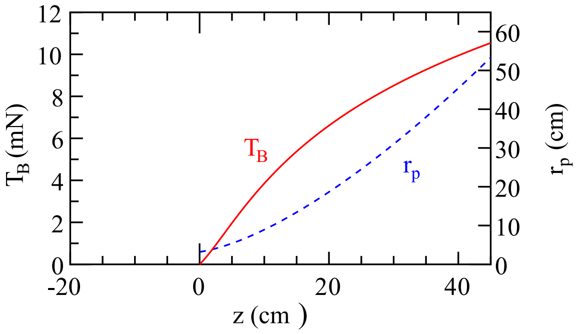

Figure 8. Axial profiles of the force component $T_{B\ \mathrm{ideal}}$ (solid line) and the plasma radius r_p (dotted line) calculated from the 1D ideal magnetic nozzle approximation and the averaged electron pressure derived from the measurements of figure 7.

with the sum of the measured three components ($T_\mathrm{s} + T_\mathrm{w} + T_B$) with an error being less than ±5%. The value of the measured T_s is independent of I_B since the maximum electron pressure is invariant with I_B as shown by the filled circles in figure 6(*a*). The directly measured value of T_s is in good agreement with the T_s value calculated from the measured electron pressure (bold solid line in figure 6(*a*)). The results validate the model which shows that the maximum electron pressure force acts on the axial source boundary [18]. Figure 6(*b*) shows that T_w is close to zero above 2 A solenoid current, validating the previous model which neglected the loss of the axial plasma momentum into the radial source boundary [20, 35], while the results with zero or weak magnetic field less than about 1 A show a negative value of T_w. The large density decay within the source cavity along the z-axis is seen for the 0 A case in figure 4(*a*), which implies a plasma potential decay from the rf antenna position to the source exit. In this situation, it is expected that ions accelerated by the electrostatic field have a significant axial velocity and ion flux lost into the radial source wall boundary is also greater, although it has not yet been quantitatively understood. In this case, significant axial momentum is lost to the radial boundary, which can be seen as the negative value of the thrust component T_w in figure 6(*b*). Figure 6(*c*) shows the increase in T_B with increasing I_B which does not affect the B_r/B_z factor in equation (3) but yields an increase in the electron pressure due to the inhibition of the cross-field diffusion (figure 4(*a*) and filled circles in figure 6(*c*)). Then the increased absolute value of $\partial p_\mathrm{e}/\partial r$ in equation (3) and the resultant increase in T_B can be obtained. The experimentally measured T_B is found to approach the theoretical upper limit $T_{B\ \mathrm{ideal}}$ shown by the horizontal bold line in figure 6(*c*) derived from the ideal one-dimensional magnetic nozzle approximation. As a result of the increased T_B, the constant T_s, and the negligible T_w, the directly measured total thrust T_total is also increased by the magnetic field strength as seen in figure 6(*d*). Hence these results show that one of the key issues in improving the performance of the helicon plasma thruster is the inhibition of cross-field diffusion in the magnetic nozzle.

Here it should be mentioned that the theoretical upper limit given by equation (5) is not that of the helicon plasma thruster, as the averaged electron pressure at the source exit, which is smaller than the maximum electron pressure in the source due to the plasma loss to the radial source wall, is used for the calculation. As the role of the magnetic nozzle (as well as the physical nozzle) is the conversion of the plasma momentum from the radial to axial directions [18, 30], inhibiting the plasma loss to the wall and guiding the plasma to the magnetic nozzle could improve the thruster performance. Furthermore, T_B calculated from the one-dimensional analysis with the approximation of $B_z(r, z) \simeq B_z(0, z)$ underestimates the value of T_B by 20–30%. Hence it is expected that some of the plasma is still lost from the magnetic nozzle even for the maximum solenoid current of 15 A in the present experiment. To capture the momentum delivered by the plasma lost from the magnetic nozzle, the physical nozzles ('nozzle 1' and 'nozzle 2' in figure 1) are attached at the thruster exit. The total thrust measured with no physical nozzle, with 'nozzle 1', and with 'nozzle 2' are plotted by open circles, filled triangles and open squares in figure 9, respectively, where the solenoid current is maintained at 15 A for all the cases. It is found that the total thrust is increased by attaching the nozzles and more thrust can be obtained for the larger nozzle (nozzle 2); the maximum thrust of 20 ± 1 mN was obtained for the 2 kW rf power. The ion saturation currents I_sat of the LP located at $z = 40$ cm and biased at −70 V are 125 μA with no physical nozzle, and 145 μA with both 'nozzle 1' and 'nozzle 2', respectively, for the rf power of 1 kW. This 16% increase in I_sat is similar to the 14% increase in thrust for nozzle 1 by significantly smaller than the 33% increase in thrust measured for nozzle 2. These data suggest that the radial momentum delivered by those ions lost from the magnetic nozzle is captured and converted into the axial force by the physical nozzle. This increase might be qualitatively similar to that observed in the conical helicon thruster [36]. It should be mentioned that the physical nozzles are electrically grounded in the present experiment and the

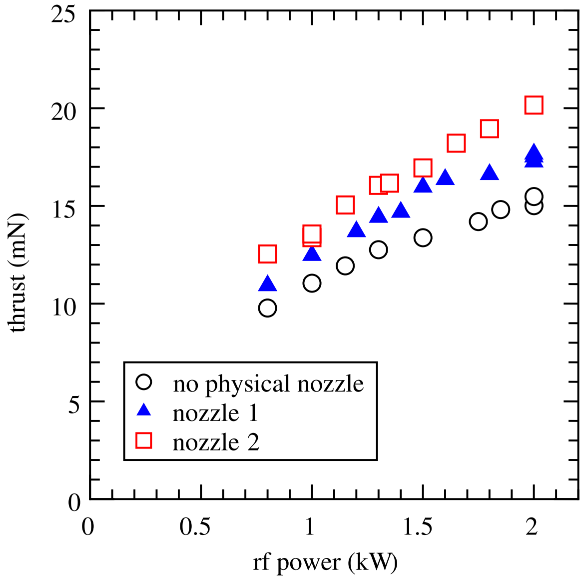

Figure 9. Total thrust T_total as a function of the rf power with 'no physical nozzle' (open circles), with 'nozzle 1' (filled triangles), and with 'nozzle 2' (open squares), respectively, where the solenoid current I_B is maintained at 15 A for all three cases. Typical error in the thrust measurement is within ±5%.

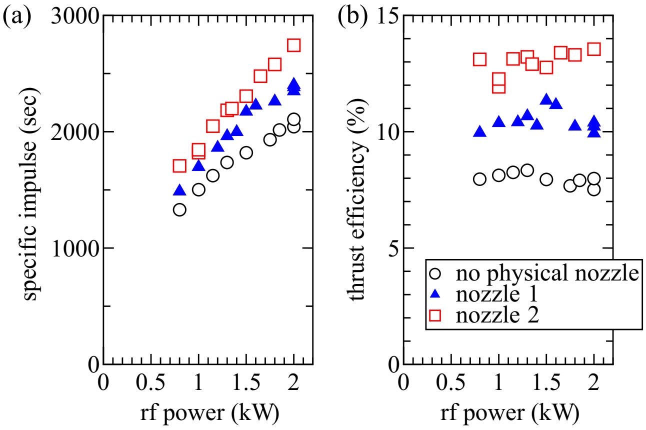

Figure 10. (*a*) Specific impulse and (*b*) thrust efficiency as a function of rf power with 'no physical nozzle' (open circles), with 'nozzle 1' (filled triangles), and with 'nozzle 2' (open squares), respectively, where these values are obtained from the measured thrust of figure 9 and the known propellant mass flow rate (0.75 mg s^{-1}). The estimated errors for the specific impulse and the thrust efficiency are ±6% and ±11%, respectively.

effect of the sheath at the inner surface of the nozzle on the thrust has not yet been verified. The comparison between the thrust for an electrically floating or a biased nozzle will be the subject of future investigations.

Two important parameters for electric propulsion device assessment are the specific impulse I_{sp} and the thrust efficiency η_T defined as $I_{sp} = T_{total}/\dot{m}g$ and $\eta_T = T_{total}^2/2\dot{m}P$, where $\dot{m}$, g and P are the mass flow rate of the propellant gas, the gravitational constant at sea level and the electric power [4]. Both the dc power for the solenoid and the rf power for the plasma production have to be included in the electric power P; however, the dc power is not included in the present assessment as the solenoid can be replaced by permanent magnets as has been demonstrated by authors [37]. I_{sp} and η_T calculated from the measured thrust in figure 9 for all the three cases (with no physical nozzle, with 'nozzle 1', and with 'nozzle 2') are plotted in figure 10 by open circles, filled triangles and open squares, respectively. The errors in I_{sp} and η_T estimated from the errors in the thrust measurement and the flow rate are ±6% and ±11%, respectively. For the case with 'nozzle 2', a maximum specific impulse of 2750±165 s is obtained yielding a thruster efficiency of 13.5 ± 1.5% for 2 kW rf power. A different helicon thruster has also been operated in a high pumping speed vacuum facility [12] and 10.8 mN thrust has been quoted for 2 kW rf power and 2.2 mg s^{-1} gas flow rate. The effect of the pumping speed and operating pressure on the helicon thruster performance have yet to be fully investigated.

5. Conclusion

The force components exerted on the axial source boundary (T_s), radial source boundary (T_w), magnetic nozzle (T_B) and the total thrust (T_{total}) imparted from the helicon plasma thruster have been independently measured for plasma conditions such that a constant plasma injection into the magnetic nozzle is maintained and some control of the plasma cross-field diffusion and expansion within the magnetic nozzle is obtained by changing the magnetic field strength. The thrust arising from the magnetic nozzle (T_B) is increased by inhibiting the cross-field diffusion and approaches the theoretical upper limit ($T_{B\ ideal}$) derived for a one-dimensional ideal magnetic nozzle approximation for maximum axial magnetic field strength of 760 G. Direct measurements of T_s and T_w validate the predicted electron pressure force onto the axial boundary and the negligible radial loss of the axial momentum when some axial magnetic field is applied (⩾50 G). Some of the momentum lost from the magnetic nozzle can be 'captured' and converted into axial momentum by adding a physical nozzle attached to the thruster exit. The maximum measured thrust is 20 ± 1 mN for 25 ± 0.25 sccm argon propellant and 2 kW rf power, giving a specific impulse of 2750 ± 165 s and a thrust efficiency of 13.5 ± 1.5%. Testing the thruster in a high pumping speed environment has yet to be fully investigated.

Acknowledgments

K Takahashi and A Ando would like to thank the late Mr Hiroyasu Ishida for his technical support. This work is partially supported by a Grant-in-Aid for Scientific Research (B 25287150) from the Japan Society for the Promotion of Science, the Sumitomo Foundation and the Hattori Hokokai Foundation.

References

[1] Sasoh A 1994 *Phys. Plasmas* **1** 464
[2] Zuin M, Cavazzana R, Martines E, Serianni G, Antoni V, Bagatin M, Andrenucci M, Paganucci F and Rossetti P 2004 *Phys. Rev. Lett.* **92** 225003
[3] Tobari H, Ando A, Inutake M and Hattori K 2007 *Phys. Plasmas* **14** 093507
[4] Goebel D M and Katz I 2008 *Fundamentals of Electric Propulsion: Ion and Hall Thrusters* (Hoboken, NJ: Wiley)
[5] Diamant K D, Pollard J E, Cohen R B, Raitses Y and Fisch N J 2006 *J. Propulsion Power* **22** 1396
[6] Scharfe M K, Gascon N, Cappelli M A and Fernandez E 2006 *Phys. Plasmas* **13** 083505
[7] Kuninaka H, Nishiyama K, Funaki I, Shimizu Y, Yamada T and Kawaguchi J 2006 *IEEE Trans. Plasma Sci.* **34** 2125
[8] Snyder J S, Goebel D M, Hofer R R, Polk J E, Wallace N C and Simpson H 2012 *J. Propulsion Power* **28** 371
[9] Longmier B W, Cassady L D, Ballenger M G, Carter M D, Chang-Díaz F R, Glover T W, Ilin A V, McCaskill G E, Olsen C S and Squire J P 2011 *J. Propulsion Power* **27** 915
[10] Charles C 2009 *J. Phys. D: Appl. Phys* **42** 163001 and references therein
[11] Batishchev O V 2009 *IEEE Trans. Plasma Sci.* **37** 1563
[12] Shabshelowitz A and Gallimore A D 2013 *J. Propulsion Power* **29** 919
[13] Pottinger S, Lappas V, Charles C and Boswell R 2011 *J. Phys. D: Appl. Phys.* **44** 235201
[14] Takahashi K *et al* 2011 *Appl. Phys. Lett.* **98** 141503
[15] Williams L T and Walker M L R 2013 *J. Propulsion Power* **29** 520
[16] Harle T, Pottinger S J and Lappas V J 2013 *Plasma Sources Sci. Technol.* **22** 015015
[17] Boswell R W and Chen F F 1997 *IEEE Trans. Plasma Sci.* **25** 1229 and references therein
[18] Fruchtman A 2006 *Phys. Rev. Lett.* **96** 065002

[19] Ahedo E and Merino M 2010 *Phys. Plasmas* **17** 073501
[20] Takahashi K, Lafleur T, Charles C, Alexander P and Boswell R W 2011 *Phys. Rev. Lett.* **107** 235001
[21] Ahedo E and Navarro-Cavallé J 2013 *Phys. Plasmas* **20** 043512
[22] Lafleur T, Takahashi K, Charles C and Boswell R W 2011 *Phys. Plasmas* **18** 080701
[23] Fruchtman A 2009 *Plasma Sources Sci. Technol.* **18** 025033
[24] Ahedo E and Merino M 2011 *Phys. Plasmas* **18** 053504
[25] Singh N, Rao S and Ranganath P 2013 *Phys. Plasmas* **20** 032111
[26] Takahashi K, Charles C and Boswell R W 2013 *Phys. Rev. Lett.* **110** 195003
[27] Roberson B R, Winglee R and Prager J 2011 *Phys. Plasmas* **18** 053505
[28] Brown S C 1967 *Basic Data of Plasma Physics* 2nd edn (Cambridge, MA: The MIT Press) chapter 2
[29] Takahashi K 2012 *Rev. Sci. Instrum.* **83** 083508
[30] Takahashi K, Lafleur T, Charles C, Alexander P and Boswell R W 2012 *Phys. Plasmas* **19** 083509
[31] Fruchtman A, Takahashi K, Charles C and Boswell R W 2012 *Phys. Plasmas* **19** 033507
[32] Arefiev A V and Breizman B N 2008 *Phys. Plasmas* **15** 042109
[33] Takahashi K, Charles C, Boswell R, Cox W and Hatakeyama R 2009 *Appl. Phys. Lett.* **94** 191503
[34] Rao S and Singh N 2012 *Phys. Plasmas* **19** 093507
[35] Fruchtman A 2008 *IEEE Trans. Plasma Sci.* **36** 403
[36] Charles C, Takahashi K and Boswell R W 2012 *Appl. Phys. Lett.* **100** 113504
[37] Takahashi K, Charles C, Boswell R and Ando A 2013 *J. Phys. D: Appl. Phys.* **46** 352001